



Solar Axions from Nuclear Transitions

Tanmoy Kumar ^{1,*} and Newton Nath ^{2,†}

¹*School of Physical Sciences, Indian Association for the Cultivation of Science,*

2A & 2B Raja S.C. Mullick Road, Jadavpur, Kolkata 700032, India

²*Department of Physics, Indian Institute of Technology (BHU), Varanasi 221005, India*

We investigate the possibility of detecting 14.4 keV and 9.4 keV solar axions and axion-like particles that could be produced in the M1 nuclear transitions of ^{57}Fe and ^{83}Kr , respectively. To do so, we used data from soft X-ray observations of the quiet Sun collected by the Solar X-ray Monitor (XSM) on board India’s Chandrayaan-2 lunar mission. We observe that although the effective axion-nucleon couplings for ^{83}Kr and ^{57}Fe differ only slightly, their fluxes differ by nearly three orders of magnitude. Consequently, the limit on $|g_{aN}^{\text{eff}} \times g_{a\gamma\gamma}|$ and only $g_{a\gamma\gamma}$ vs. m_a provide more than an order-of-magnitude stronger constraint for Fe than for Kr.

I. INTRODUCTION

The *strong CP problem*, a longstanding unanswered puzzle in the Standard Model (SM) of particle physics, arises from the fact that charge conjugation-parity (CP) symmetry is expected to be violated in quantum chromodynamics (QCD), yet no such violation has been observed experimentally. One of the most elegant solutions to this problem is the introduction of an anomalous global $U(1)$ symmetry, known as the Peccei-Quinn (PQ) symmetry, which is spontaneously broken. This mechanism gives rise to a pseudo-Nambu-Goldstone boson (pNGB) called the QCD axion [1–3]. At present, the axion remains one of the best-motivated elementary particles beyond the SM (BSM). In addition to offering the most appealing explanation to the strong CP problem, axions are also excellent dark matter candidates [4–11]. The theoretical framework admits a large variety of QCD axion models, each characterized by distinctive phenomenological features. For a comprehensive review, see Ref. [12] and references therein. Apart from QCD axions, a broader class of pseudoscalar bosons, called axion-like particles (ALPs), emerges in many BSM scenarios [13]. Now onwards, we will use the term “axions” to refer to both axions and ALPs. Due to their compelling theoretical motivation, a massive effort is underway to search for these elusive axions, and these searches are probing a substantial section of the parameter space [14–16]. This creates

* kumartanmoy1998@gmail.com

† nnath.phy@iitbhu.ac.in

significant excitement for the possible discovery of such BSM particles in the next decade [17, 18]. For recent reviews, see Refs. [12, 15, 18–22] and the references therein. In addition, current axion experimental limits can be found in [23].

In particular, astrophysical searches for these elusive particles have gained prominence over the last few years. Astrophysical objects such as stars, supernovae, quasars, etc., in lieu of their extreme temperatures and densities, act as efficient factories of these axions. Using the observation of such objects via highly sensitive telescopes across a wide range of frequencies, some of the most stringent constraints on the interaction of these axions with the SM particles have been obtained. For an overview of the latest constraints, see [23]. A particularly important target for these astrophysical axion searches is the Sun. In the dense solar core, where temperatures ~ 1 keV, axions with masses below a few keV can be efficiently produced via their coupling to photons through the Primakoff effect [24, 25] and photon-axion conversion in solar magnetic fields [26–28], as well as via their coupling to electrons through electron-nucleus scattering, electron-electron bremsstrahlung, and Compton processes [29]. Updated rates are provided in [30]. The CERN Axion Solar Experiment (CAST) [31] has searched for these solar axions and, in the absence of any signal, has placed a tight constraint on axions’ coupling to photons ($g_{a\gamma\gamma}$), excluding $g_{a\gamma\gamma} > 0.66 \times 10^{-10} \text{ GeV}^{-1}$ at 95% confidence level for axions with mass $m_a \lesssim 0.02$ eV. A similar bound can be obtained from observations of horizontal branch (HB) stars in globular clusters [32, 33]. Recently, authors of [34] have found a slightly stronger bound, specifically $g_{a\gamma\gamma} \lesssim 0.34 \times 10^{-10} \text{ GeV}^{-1}$ for $m_a < 1$ keV, by measuring the ratio of stars in the asymptotic giant branch and in the HB in globular clusters.

Apart from photons and electrons, in most of the theoretically well-motivated scenarios, axions also interact with nucleons such as neutrons and protons. This presents the possibility that axions can be produced from the de-excitation of thermally excited nuclei of elements present in the core of the Sun. The Sun, being a Population I star, has a significant abundance of heavy elements ¹, which have been either synthesized through nuclear reactions occurring in the solar interior or inherited as remnants of the primordial molecular cloud from which the solar system formed. Among these, odd- A nuclei possessing low-lying excited states with excitation energies of a few keV can be thermally excited via the absorption of photons in the hot solar plasma. The subsequent de-excitation can proceed through the emission of monoenergetic axions carrying energies equal to the transition energy between the excited and ground states. These are magnetic dipole (M1) transitions, first discussed in the context of axion emission in Ref. [35]. A comprehensive list of nuclides with such low-lying M1 transitions in the keV energy range is given in Table I of Ref. [36]

¹ By heavy elements we mean elements heavier than hydrogen.

along with the respective nuclear parameters and the energy of the transition. Of the elements listed therein, those with significant abundance in the solar core are ${}^3\text{He}$, ${}^7\text{Li}$, ${}^{57}\text{Fe}$, and ${}^{83}\text{Kr}$. Solar axions produced via the nuclear de-excitation of these isotopes have been the subject of experimental searches over the years.

Experimental searches for the resonant absorption of solar axions emitted via nuclear M1 transitions have been carried out using ${}^7\text{Li}$ [37–40], ${}^{57}\text{Fe}$ [41–44], and ${}^{83}\text{Kr}$ [45, 46] as target nuclei. The sensitivity of helioscopes to various nuclear axion production channels has been recently assessed in Refs. [40, 43, 47]. Data from the SNO experiment place a bound on the isotriplet axion–nucleon coupling g_{3aN} , excluding $g_{3aN} \gtrsim 2 \times 10^{-5}$ at 95% confidence level [48]. The production of 5.49 MeV monochromatic solar axions from the M1 nuclear transition of excited ${}^3\text{He}^*$ produced via the nuclear fusion reaction $p + d \rightarrow {}^3\text{He}^*$ was first calculated in Ref. [49]. The Borexino experiment subsequently constrained such axions, placing bounds on the coupling combinations (g_{3aN}, g_{ae}) and $(g_{3aN}, g_{a\gamma})$ [50]. More recently, the sensitivity of JUNO to these 5.49 MeV axions has been examined in Ref. [51], where it is shown that JUNO could improve upon the Borexino constraint by approximately an order of magnitude, owing to its superior energy resolution.

In this work, we conduct a search for solar axions emitted via the M1 nuclear de-excitation of ${}^{57}\text{Fe}$ and ${}^{83}\text{Kr}$. Recent solar abundance studies [52] have highlighted a significant abundance of ${}^{57}\text{Fe}$ as well as a non-zero abundance of ${}^{83}\text{Kr}$ in the solar core. As listed in Table I of Ref. [36], both isotopes possess low-lying M1 excitation viz., ${}^{57}\text{Fe}$ has an excitation at 14.4 keV, while ${}^{83}\text{Kr}$ has an excitation at 9.4 keV. In the hot solar plasma, a fraction of these nuclei can be thermally excited to these low-lying states which can subsequently de-excite via axion emission, yielding monochromatic axions at 14.4 keV and 9.4 keV for ${}^{57}\text{Fe}$ and ${}^{83}\text{Kr}$, respectively. Such solar axions have been searched for in several experiments, including CAST [43] and CUORE [44] for the 14.4 keV ${}^{57}\text{Fe}$ channel via photon conversion and the axio-electric effect, respectively, and at the Baksan Neutrino Observatory for the 9.4 keV ${}^{83}\text{Kr}$ channel via resonant nuclear absorption [46].

We investigate such axions using soft X-ray observations of the quiet Sun by the Chandrayaan-2 spacecraft. Chandrayaan-2 is a lunar orbiter of the Indian Space Research Organization (ISRO), launched in 2019 into an orbit around the Moon. Among its scientific payloads is the Solar X-ray Monitor (XSM), which records solar X-ray spectra in the 1–15 keV energy range. During the 2019–2020 solar minimum [53, 54], when solar activity was at its lowest, XSM recorded high-quality quiet-Sun soft X-ray spectra. The observed spectrum is dominated by two components: the quiescent coronal emission and the emission from flaring plasma. In addition, if axions are produced in the solar interior, they can convert into photons in the solar magnetic field, thereby contributing

additional spectral features to the observed soft X-ray spectrum. Previously Ref. [55] searched for X-ray photons arising from the conversion of solar axions produced via the Primakoff effect, Compton scattering, and bremsstrahlung processes in the solar magnetic field, using Chandrayaan-2 data to set an upper bound on the axion-photon coupling. A similar analysis was previously performed using NuSTAR data [56]. In the present work, we utilize the same Chandrayaan-2 solar soft X-ray dataset to search for monochromatic 14.4 keV and 9.4 keV photons arising from the conversion of ^{57}Fe and ^{83}Kr nuclear axions in the solar magnetic field, and in the absence of such spectral features, we derive upper limits on the axion-nucleon and axion-photon couplings.

The remainder of this paper is organized as follows. In Sec. II, we discuss solar axion production and fluxes of the nuclei. Sec. III deals with conversion of axions to photons. Numerical analysis using the likelihood method for Chandrayaan-2 data and our limit on various axion couplings are discussed in Sec. IV. Finally, our concluding remarks are presented in Sec. V.

II. SOLAR AXIONS FROM NUCLEAR TRANSITION

The production and detection of axions are governed by their couplings to SM fields. The effective low-energy Lagrangian relevant for our analysis is given by [51]

$$\mathcal{L} = \frac{1}{2} \partial_\mu a \partial^\mu a - m_a^2 a^2 - \frac{1}{4} g_{a\gamma\gamma} a F_{\mu\nu} \tilde{F}^{\mu\nu} - ia \bar{N} \gamma_5 (g_{0aN} + \tau_3 g_{3aN}) N, \quad (1)$$

where the first two terms are the kinetic and mass terms of the axion field a , $F_{\mu\nu}$ and $\tilde{F}^{\mu\nu}$ are the electromagnetic field strength tensor and its dual, and $N = (p, n)^T$ is the proton-neutron isospin doublet. The parameter m_a denotes the axion mass, $g_{a\gamma\gamma}$ is the axion-photon coupling, and g_{0aN} and g_{3aN} are the iso-singlet and iso-triplet axion-nucleon couplings, respectively. As will be discussed later, axion production in the solar core proceeds via the nucleon couplings g_{0aN} and g_{3aN} , while detection relies on the conversion of axions into photons through the coupling $g_{a\gamma\gamma}$.

Apart from the standard de-excitation via photon emission, a nucleus in an excited state can alternatively decay to its ground state by emitting an axion. For the low-lying nuclear excited states of ^{57}Fe and ^{83}Kr we are concerned with, this process proceeds via a magnetic dipole (M1) transition, in which the axion carries away the full transition energy as a monochromatic signal. Specifically, for ^{57}Fe the ground state has total angular momentum $J_0 = 1/2$ and the first excited state has $J_1 = 3/2$, while for ^{83}Kr the ground state has $J_0 = 9/2$ and the first excited state has $J_1 = 7/2$ [47]. In both cases, the change in angular momentum $|\Delta J| = 1$ is consistent with an M1 transition.

For such an M1 transition, the ratio of the transition rates for axion emission (Γ_a) and photon emission (Γ_γ) is given by [57]

$$\frac{\Gamma_a}{\Gamma_\gamma} = \left(\frac{k_a}{k_\gamma}\right)^3 \frac{1}{2\pi\alpha_{\text{EM}}} \frac{1}{1+\delta^2} \left[\frac{\beta g_{0aN} + g_{3aN}}{(\mu_0 - \frac{1}{2})\beta + \mu_3 - \eta} \right]^2. \quad (2)$$

Here, k_a and k_γ are the axion and photon momenta, respectively. For axion masses $m_a \ll 1$ eV, we have $k_a = \sqrt{E_a^2 - m_a^2} \simeq E_a$ where E_a is the axion energy and is equal to the energy of the M1 nuclear transition. Since the energy of the M1 nuclear transition is fixed, an axion and a photon emitted during the transition will have the same energy $E_a = E_\gamma = k_\gamma$. Thus we have $k_a/k_\gamma \simeq 1$. The quantity α_{EM} is the electromagnetic fine-structure constant, $\mu_0 = \mu_p + \mu_n \approx 0.88$ and $\mu_3 = \mu_p - \mu_n \approx 4.77$ are the isoscalar and isovector nuclear magnetic moments expressed in units of the nuclear magneton, and δ is the E2/M1 multipole mixing ratio of the transition. The parameters β and η encode the nuclear structure of the isotope and their values are tabulated in Ref. [36]. The branching ratio Γ_a/Γ_γ (Eq. (2)) quantifies the probability that a given nuclear transition proceeds via axion emission rather than photon emission.

For ^{57}Fe , substituting the values $\delta = 0.002$, $\beta = -1.19$, and $\eta = 0.8$ from Ref. [36] into Eq. (2), we obtain

$$\frac{\Gamma_a}{\Gamma_\gamma} = 1.82 (-1.19 g_{0aN} + g_{3aN}) \equiv 1.82 g_{aN, \text{Fe}}^{\text{eff}}, \quad (3)$$

where we have defined the effective coupling $g_{aN, \text{Fe}}^{\text{eff}} = -1.19 g_{0aN} + g_{3aN}$. Similarly, for ^{83}Kr , using $\delta = 0.002$, $\beta = -1$, and $\eta = 0.5$ from Ref. [36], we find

$$\frac{\Gamma_a}{\Gamma_\gamma} = -g_{0aN} + g_{3aN} \equiv g_{aN, \text{Kr}}^{\text{eff}}, \quad (4)$$

where $g_{aN, \text{Kr}}^{\text{eff}} = -g_{0aN} + g_{3aN}$. We note that the two effective couplings are numerically similar, $g_{aN, \text{Fe}}^{\text{eff}} \simeq g_{aN, \text{Kr}}^{\text{eff}}$, differing only through the isotope-specific coefficient multiplying g_{0aN} .

To calculate the flux of solar axions produced via the nuclear de-excitation of ^{57}Fe and ^{83}Kr , we follow the procedure outlined in Refs. [41, 47]. The axion emission rate per unit mass of the Sun is given by

$$\mathcal{N}_a(r) = \mathcal{N}(r) \omega_1(T(r)) \frac{1}{\tau_0} \frac{1}{1+\alpha} \frac{\Gamma_a}{\Gamma_\gamma}, \quad (5)$$

where $\mathcal{N}(r)$ is the number of relevant nuclei per unit mass of the Sun, $\omega_1(T(r))$ is the thermal population fraction of the excited state at local temperature T , given by the Boltzmann factor

$$\omega_1(T(r)) = \frac{(2J_1 + 1) e^{-E_1/T(r)}}{(2J_0 + 1) + (2J_1 + 1) e^{-E_1/T(r)}}, \quad (6)$$

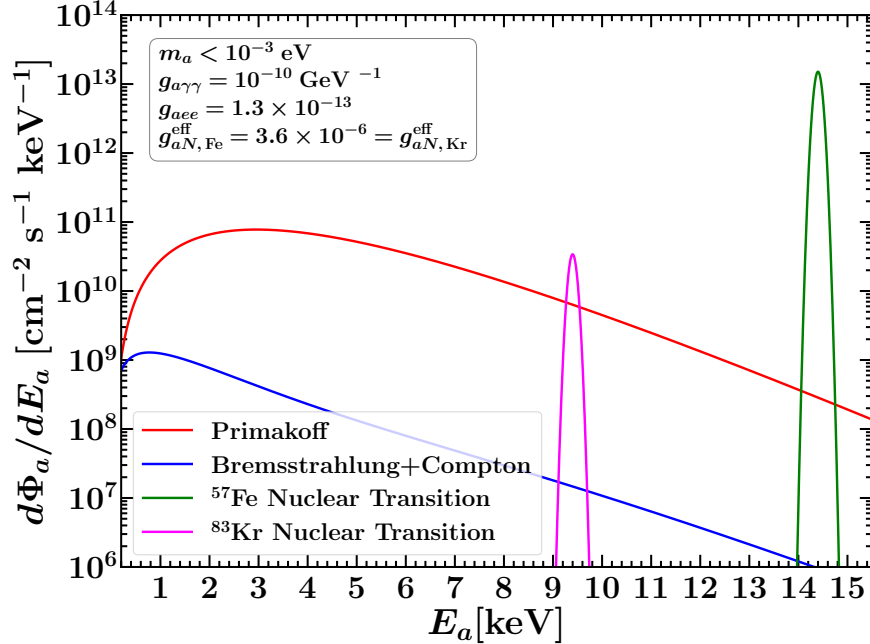


FIG. 1. Differential solar axion flux at Earth from various production mechanisms. The continuous spectra include the Primakoff component (red) and the electron-induced contributions—bremsstrahlung and Compton (blue). The line-like spectra are from the 14.4 keV M1 nuclear transition of ^{57}Fe (green) and the 9.4 keV M1 nuclear transition of ^{83}Kr (magenta). For visualization purposes, the monoenergetic lines are convolved with a Gaussian corresponding to the XSM energy resolution.

with J_0 and J_1 being the angular momenta of the ground and excited states, respectively, and E_1 the transition energy. The quantity τ_0 is the mean lifetime of the nuclear excited state, α is the internal conversion coefficient which is the ratio of the number of nuclei undergoing de-excitation via photon emission to the number of nuclei undergoing de-excitation via electron emission, and Γ_a/Γ_γ is the axion-to-photon branching ratio defined in Eq. (2).

The number of relevant nuclei per unit mass of the Sun can be written as

$$\mathcal{N}(r) = \frac{X_H(r)}{m_p} 10^{\varepsilon-12} \mathcal{A}, \quad (7)$$

where $X_H(r)$ is the local hydrogen mass fraction, m_p is the proton mass, ε is the logarithmic photospheric abundance of the parent element (Fe or Kr) relative to hydrogen in the standard astronomical scale $\log_{10}(n_{\text{element}}/n_H) + 12$ which we have adopted from [52], and \mathcal{A} is the isotopic abundance fraction of the specific isotope (^{57}Fe or ^{83}Kr) which we have adopted from [47].

The axion emission rate per unit volume at radius r is then $\rho(r)\mathcal{N}_a(r)$, where $\rho(r)$ is the local mass density of the solar plasma. The total axion luminosity of the Sun is obtained by integrating

this quantity over the full solar volume,

$$L_a = \int_0^{R_\odot} \rho(r) \mathcal{N}_a(r) 4\pi r^2 dr. \quad (8)$$

Assuming isotropic emission, the differential flux of solar axions at Earth (distance d_\odot from the Sun) is

$$\Phi_a = \frac{L_a}{4\pi d_\odot^2}. \quad (9)$$

Combining the expressions above, the total solar axion flux at Earth from the nuclear de-excitation of a given isotope is

$$\Phi_a = \frac{a 10^{\varepsilon-12}}{4\pi d_\odot^2} \cdot \frac{1}{\tau_0 (1 + \alpha)} \cdot \frac{\Gamma_a}{\Gamma_\gamma} \cdot \underbrace{\int_0^{R_\odot} \omega_1(T(r)) \frac{\rho(r) X_H(r)}{m_p} 4\pi r^2 dr}_{\equiv \mathcal{I}}, \quad (10)$$

where all nuclear parameters are isotope-specific and the dimensionless integral \mathcal{I} encodes the thermal and compositional structure of the solar interior. \mathcal{I} is evaluated numerically using the B23-AGSS09 standard solar model from [58], which provides radial profiles of $T(r)$, $\rho(r)$, and $X_H(r)$.

Substituting the respective nuclear parameters into Eq. (10), the axion fluxes from the 14.4 keV transition of ^{57}Fe and the 9.4 keV transition of ^{83}Kr at Earth read as

$$\Phi_a^{\text{Fe}} = \Phi_0^{\text{Fe}} \left(g_{aN, \text{Fe}}^{\text{eff}} \right)^2, \quad (11)$$

$$\Phi_a^{\text{Kr}} = \Phi_0^{\text{Kr}} \left(g_{aN, \text{Kr}}^{\text{eff}} \right)^2, \quad (12)$$

where

$$\Phi_0^{\text{Fe}} = 2.18 \times 10^{23} \text{ cm}^{-2} \text{ s}^{-1} \text{ and } \Phi_0^{\text{Kr}} = 4.92 \times 10^{20} \text{ cm}^{-2} \text{ s}^{-1}. \quad (13)$$

As is evident from Eq. (13), the ^{83}Kr axion flux is roughly three orders of magnitude smaller than that of ^{57}Fe . This suppression is predominantly due to the much lower photospheric abundance of krypton relative to iron, $\varepsilon_{\text{Kr}} \approx 3.12$ versus $\varepsilon_{\text{Fe}} \approx 7.46$ [52], which translates directly into a correspondingly smaller number of emitting nuclei in the solar interior.

These monoenergetic axion fluxes are displayed in Fig. 1, where the green and magenta lines correspond to the 14.4 keV and 9.4 keV lines from the M1 nuclear transitions of ^{57}Fe and ^{83}Kr , respectively. For comparison, we also show the continuous axion spectra from the Primakoff process (red) and the combined electron bremsstrahlung and Compton contributions (blue).

III. X-RAY FLUX FROM AXION-PHOTON CONVERSION OUTSIDE THE SUN

A fraction of the axions produced in the solar interior can convert into photons as they traverse the Sun's external magnetic field, via the inverse Primakoff process [59]. For the monoenergetic axions considered here, this conversion yields a flux of X-ray photons at the same energies as the parent nuclear transitions, 14.4 keV for ^{57}Fe and 9.4 keV for ^{83}Kr , arriving at Earth as sharp spectral lines superimposed on the solar X-ray background. An X-ray telescope observing the Sun can therefore search for these line features in the detected spectrum, and the non-observation of any such excess can be used to place constraints on the product of the axion-nucleon and axion-photon couplings, $|g_{aN}^{\text{eff}} \times g_{a\gamma\gamma}|$.

To calculate the intensity of these X-rays, we start by calculating the conversion probability of axions into photons while traveling through a magnetized plasma. In the presence of an external magnetic field $\mathbf{B}(\ell)$, in this case the solar magnetic field, axions mix with the component of the photon field which is polarized parallel to the external magnetic field [59] resulting in axion-photon oscillation. The equation of motion for axions in a magnetized plasma is given by [59]

$$\left((E_a - i\partial_\ell)\mathbb{I} + \hat{M}(\ell) \right) \begin{pmatrix} A_{\parallel}(\ell) \\ a(\ell) \end{pmatrix} = 0, \quad (14)$$

where A_{\parallel} represents the photon polarization state parallel to $\mathbf{B}_T(\ell)$ where, $\mathbf{B}_T(\ell)$ is the transverse projection of the external magnetic field $\mathbf{B}(\ell)$, and $\hat{M}(\ell)$ represents a 2×2 mixing matrix, given by

$$\hat{M}(\ell) = \begin{pmatrix} -\frac{\omega_p^2(\ell)}{2\omega} - i\frac{\Gamma(\ell)}{2} & g_{a\gamma\gamma} \frac{B_T(\ell)}{2} \\ g_{a\gamma\gamma} \frac{B_T(\ell)}{2} & -\frac{m_a^2}{2\omega} \end{pmatrix}, \quad (15)$$

where $\omega_p(\ell) = \sqrt{4\pi\alpha n_e(\ell)/m_e}$ represents the plasma frequency of the photon with $n_e(\ell)$ being the electron density of the plasma. In this case the plasma present in the solar atmosphere and $B_T(\ell) = |\mathbf{B}_T(\ell)|$. Here, $\Gamma(\ell) = \sum_{Z=1}^{30} n_Z(\ell) \sigma_Z$ is the absorption coefficient of the X-ray photon in the plasma with n_Z being the number density of element of atomic number Z and σ_Z being the total attenuation cross-section of a photon passing through a gas of atomic number Z . To calculate the conversion probability, we solve the equation of motion (14) subject to initial conditions at $\ell = 0$ which in our case we consider to be the solar surface. The solution at some location at a distance $\ell = h$ from the initial point is given by the path-ordered transfer matrix [59, 60],

$$\begin{pmatrix} A_{\parallel}(h) \\ a(h) \end{pmatrix} = \mathcal{P}_\ell \left[\exp \left(-iE_a h \mathbb{I} - i \int_0^h \hat{M}(\ell) d\ell \right) \right] \begin{pmatrix} A_{\parallel}(0) \\ a(0) \end{pmatrix}, \quad (16)$$

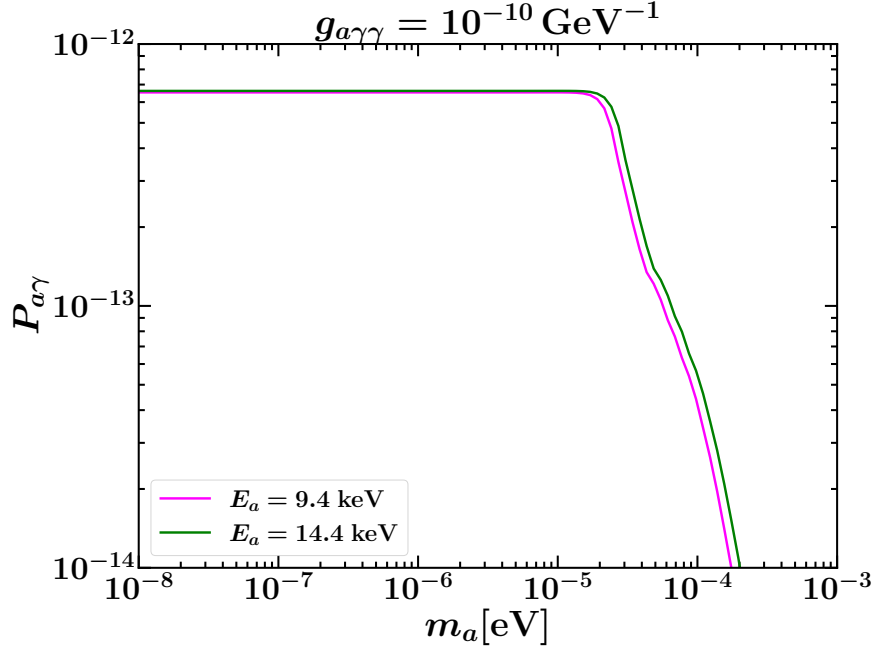


FIG. 2. Axion to photon oscillation probability at a far away distance from the Sun as a function of m_a for $E_a = 9.4$ keV (magenta solid line) and $E_a = 14.4$ keV (green solid line.)

where $A_{\parallel}(0)$ and $a(0)$ are the initial photon and axion field amplitudes, respectively, \mathbb{I} is the 2×2 identity matrix, $\hat{M}(\ell)$ is the mixing matrix encoding the local plasma and magnetic field properties, and \mathcal{P}_{ℓ} denotes path ordering along the propagation direction.

Taking the initial conditions at the solar surface to be $A_{\parallel}(0) = 0$ and $a(0) = 1$, i.e. a pure axion state with no photon admixture, the transfer matrix in Eq. (16) can be evaluated perturbatively in powers of $g_{a\gamma\gamma}$ [59]. To first order in perturbation theory, the axion-to-photon conversion probability reads

$$P_{a\gamma}(h, E_a, m_a, g_{a\gamma\gamma}) = \frac{g_{a\gamma\gamma}^2}{4} e^{-\int_0^h d\ell \Gamma(\ell)} \left| \int_0^h d\ell B_{\Gamma}(\ell) \exp \left[i \int_0^{\ell} d\ell' q(\ell') + \frac{1}{2} \int_0^{\ell} d\ell' \Gamma(\ell') \right] \right|^2, \quad (17)$$

where $q(\ell) = (\omega_p^2(\ell) - m_a^2)/2E_a$ is the momentum transfer between the axion and photon.

To obtain the X-ray signal intensity at Earth, we numerically evaluate Eq. (17) using the solar magnetic field and electron density profiles adopted in Ref. [56], which extend to a heliocentric distance of $h = 29 R_{\odot}$ and we therefore perform the integration out to this distance. The photon absorption coefficient $\Gamma(\ell)$ is computed by summing contributions from all elements up to atomic number $Z = 30$, weighted by their local abundances in the solar atmosphere as tabulated in the CHIANTI atomic database [61, 62], accessed via the ChiantiPy interface [63]. For each element, we

use the total photon attenuation cross-section including coherent scattering from the NIST XCOM database [64].

Fig. 2 shows the conversion probability of axion to photon $P_{a\gamma}$, evaluated at $h = 29 R_\odot$, as a function of the axion mass m_a for the two transition energies, namely 14.4 keV (green) and 9.4 keV (magenta), respectively. In the low-mass regime, $m_a \lesssim 10^{-5}$ eV, the conversion probability is constant, while for $m_a \gtrsim 10^{-5}$ eV it falls rapidly. This behavior of the oscillation probability critically depends on the momentum exchange between the axion and the photon $q(\ell)$, which dictates the phase difference between the axion and the photon waves. The momentum transfer defines the oscillation length, $L_{\text{osc}} = 2\pi/q$, over which the waves drift out of phase. Optimal conversion requires that the spatial extent of the magnetic field is much smaller than the oscillation length, ensuring constructive interference (coherence).

For $m_a \lesssim 10^{-5}$ eV the relevant conversion region lies in the solar corona ($h \gtrsim 10^{-2} R_\odot$, see Fig. 2 of Ref. [56]), where the free-electron density is very low. As a consequence, the plasma frequency is extremely small, $\omega_p \sim 10^{-8}$ eV, as well as the photon absorption coefficient Γ is negligible, rendering the medium essentially transparent to X-rays. Since both m_a and ω_p are far below the photon energy, the momentum transfer $q \rightarrow 0$ and the oscillation length $L_{\text{osc}} = 2\pi/q$ become much larger than the physical extent of the corona. The phase factor in Eq. (17) therefore approaches unity, meaning the axion and photon waves remain perfectly in phase across the entire coronal volume. In this fully coherent, low-absorption regime, the conversion probability simplifies to

$$P_{a\gamma} \propto \left(g_{a\gamma\gamma} \int_0^h d\ell B_T(\ell) \right)^2, \quad (18)$$

which is independent of m_a , giving rise to the characteristic flat plateau seen in Fig. 2. Although the coronal field is weak, the large integration length and perfect coherence are sufficient to dominate the signal.

For $m_a \gtrsim 10^{-5}$ eV, the conversion probability is suppressed by two competing effects. Firstly for these masses the resonance condition $m_a \simeq \omega_p$ is satisfied in the chromosphere or photosphere (see Fig. 2 of Ref. [56]), where the magnetic field is strong ($B \sim 10^2$ G) but the plasma density and thereby the free electron and ion density is also very high. Since the absorption coefficient scales with the free electron and ion density the optical depth in these layers is very large, and any photons produced by resonant conversion are rapidly reabsorbed before escaping. Secondly, in the overlying transparent corona where $m_a \gg \omega_p$, the momentum transfer grows as $q \approx m_a^2/2E_a$, driving L_{osc} well below the coronal scale. The axion and photon waves quickly dephase, and the conversion becomes incoherent. These two effects namely opacity suppression at the deep-

atmosphere resonance and phase mismatch in the corona, combine to produce the steep fall-off of $P_{a\gamma}$ at higher masses. The threshold at $m_a \sim 10^{-5}$ eV therefore marks the physical boundary between the chromosphere and the corona, and the shape of $P_{a\gamma}(m_a)$ is a direct map of the solar atmosphere's structure.

Given the conversion probability, the X-ray photon flux at Earth from axion-photon conversion is obtained by multiplying the solar axion flux by $\hat{P}_{a\gamma}$,

$$\Phi_\gamma(E) = \Phi_a \times \delta(E - E_a) \times \hat{P}_{a\gamma}(E, m_a, g_{a\gamma\gamma}), \quad (19)$$

where E_a is the energy of the monoenergetic axions $\hat{P}_{a\gamma}(E, m_a, g_{a\gamma\gamma}) \equiv P(h = 29 R_\odot, E, m_a, g_{a\gamma\gamma})$ is the conversion probability evaluated at the outer boundary of the integration domain. The δ -function encodes the line-like shape of the spectra.

IV. LIMITS FROM CHANDRAYAAN-2

Chandrayaan-2 is a lunar exploration mission developed by the Indian Space Research Organization and launched in July 2019 to study the composition of the lunar surface. During the 2019-2020 solar minimum, the Solar X-ray Monitor (XSM) onboard the Chandrayaan-2 observed the integrated solar X-ray spectrum originating from the entire solar disk in the 1 – 15 keV energy range in two observing seasons [65, 66]. The cumulative data from these two observing seasons of the XSM have previously been used to search for solar axions produced via Primakoff and electron-induced processes in [55]. We use the same data to search for the 14.4 keV and 9.4 keV axion lines produced from M1 nuclear transitions of ^{57}Fe and ^{83}Kr , respectively. For our analysis, we directly utilize the background-subtracted residual spectra previously derived in [55]. The data were processed using three distinct background subtraction schemes, which we designate as Case 1 (Conservative), Case 2 (Realistic), and Case 3 (Optimistic). We derive the limits for each of these three datasets separately. For full details regarding the subtraction procedures see [55].

1. **Case 1 (Conservative):** Data from which only the cosmic X-ray background was subtracted, while actively excluding bright X-ray sources and energetic solar events (large SEP events).
2. **Case 2 (Realistic):** Data from which the measured XSM background (recorded when the Sun was outside the XSM field-of-view) was subtracted, while excluding multiple bright X-ray sources and large SEP events.

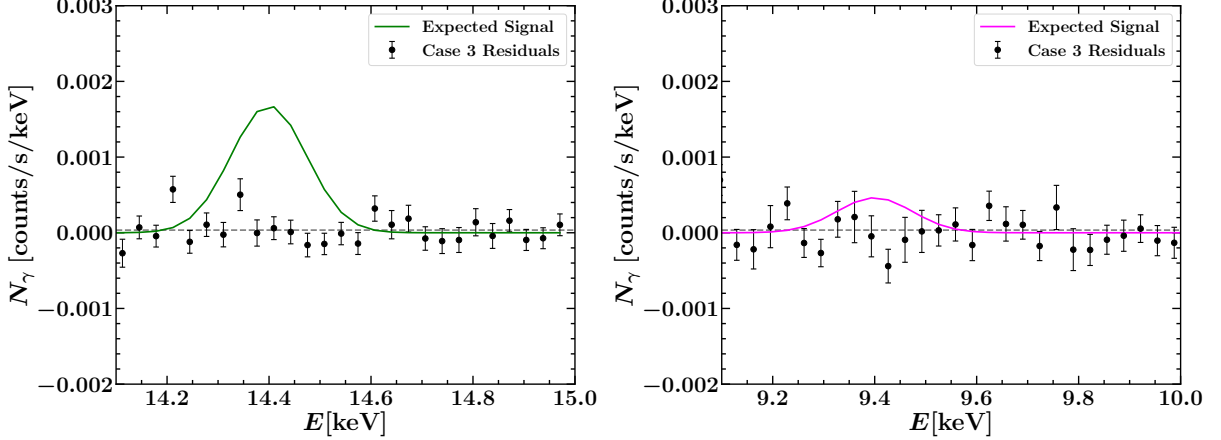


FIG. 3. The expected solar axion-induced photon signal from the 14.4 keV ^{57}Fe transition for $|g_{aN,\text{Fe}}^{\text{eff}} \times g_{a\gamma\gamma}| = 10^{-16} \text{ GeV}^{-1}$ (*left panel*) and from the 9.4 keV ^{83}Kr transition for $|g_{aN,\text{Kr}}^{\text{eff}} \times g_{a\gamma\gamma}| = 10^{-15} \text{ GeV}^{-1}$ (*right panel*) and the residual spectrum after background subtraction for Case 3. The axion signal is shown after convolution with the detector energy resolution, while the residuals represent the difference between the observed spectrum and the best-fit background model in the corresponding energy window.

3. **Case 3 (Optimistic):** Data where the spectrum obtained in Case 1 was subtracted, under the assumption that it represents the ideal background.

In both panels of Fig. 3 we show the bin-wise background-subtracted residual spectra from the Chandrayaan-2 quiet Sun observations obtained from the optimistic (Case 3) background subtraction as black dots with the associated error bars. For details see caption of Fig. 3.

To construct the theoretical signal, we begin with the X-ray photon flux $\Phi_\gamma(E)$ derived in Eq. (19), which contains a δ -function encoding the monoenergetic nature of the emission. To account for the finite energy resolution of the XSM, we replace this δ -function with a Gaussian of width $\sigma = \text{FWHM}/(2\sqrt{2\ln 2})$, with $\text{FWHM} = 175 \text{ eV}$ [65]. The expected photon counts in the i -th energy bin are then obtained by folding with the energy-dependent effective area $A_{\text{eff}}(E)$,

$$N_{\gamma,\text{exp}}(E_i) = \Phi_a \cdot \hat{P}_{a\gamma}(E_i, m_a, g_{a\gamma\gamma}) \cdot \frac{A_{\text{eff}}(E_i)}{\sqrt{2\pi}\sigma} \exp\left[-\frac{(E_i - E_a)^2}{2\sigma^2}\right], \quad (20)$$

where $E_a = 14.4(9.4) \text{ keV}$ for ^{57}Fe (^{83}Kr) and Φ_a is given in Eq. (13). Denoting the coupling-dependent overall normalization as

$$\begin{aligned} N_S(E_i) &\equiv \Phi_a \cdot \hat{P}_{a\gamma}(E_i, m_a, g_{a\gamma\gamma}) \cdot A_{\text{eff}}(E_i) \\ &= (g_{aN,\text{Fe/Kr}}^{\text{eff}} \times g_{a\gamma\gamma})^2 \cdot \Phi_0^{\text{Fe/Kr}} \cdot \hat{P}_{a\gamma}(E_i, m_a, g_{a\gamma\gamma} = 1) \cdot A_{\text{eff}}(E_i), \end{aligned} \quad (21)$$

we have

$$N_{\gamma,\text{exp}}(E_i) = N_S(E_i) \cdot \frac{1}{\sqrt{2\pi}\sigma} \exp\left[-\frac{(E_i - E_a)^2}{2\sigma^2}\right]. \quad (22)$$

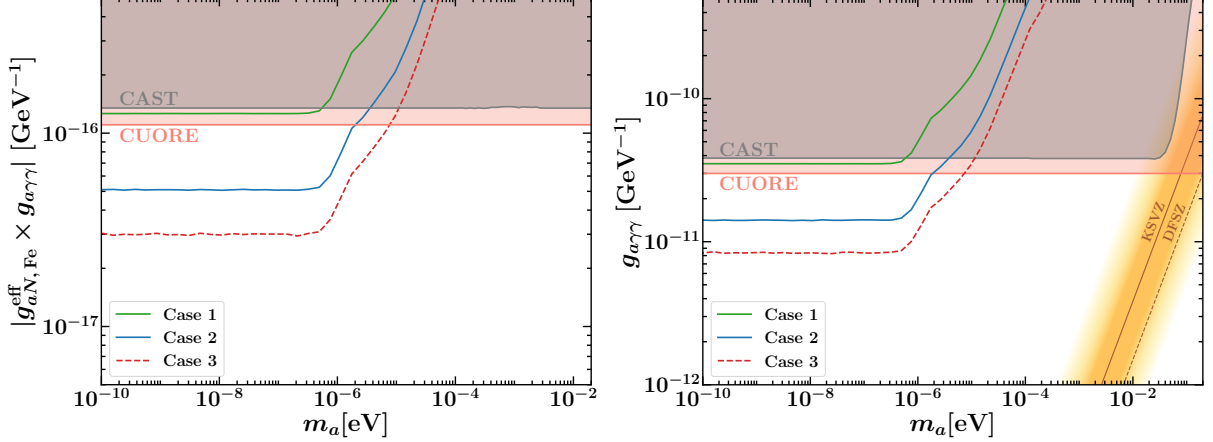


FIG. 4. Upper limits at 95% confidence level on the product $|g_{aN, \text{Fe}}^{\text{eff}} \times g_{a\gamma\gamma}|$ (left panel) and $g_{a\gamma\gamma}$ for $g_{aN, \text{Fe}}^{\text{eff}} = 3.6 \times 10^{-6}$ (right panel) as a function of the axion mass, derived from Chandrayaan-2 XSM observations. The constraint is obtained from the non-observation of an excess at the 14.4 keV ^{57}Fe nuclear transition in the solar X-ray spectrum. The yellow region represents the QCD axion band [23].

Given the observed count rate per unit energy $N_{\gamma, \text{obs}}(E_i)$ for a particular background subtraction scheme, we construct a Gaussian likelihood over all energy bins in the range 3.4–15 keV,

$$\mathcal{L}(|g_{aN}^{\text{eff}} \times g_{a\gamma\gamma}|; m_a) \propto \prod_i \exp\left[-\frac{1}{2} \left(\frac{N_{\gamma, \text{exp}}(E_i) - N_{\gamma, \text{obs}}(E_i)}{\tilde{\sigma}(E_i)}\right)^2\right], \quad (23)$$

where $\tilde{\sigma}(E_i)$ denotes the uncertainty in the observed counts. To derive constraints in the m_a – $|g_{aN}^{\text{eff}} \times g_{a\gamma\gamma}|$ plane, we adopt a uniform prior $|g_{aN}^{\text{eff}} \times g_{a\gamma\gamma}| \in [10^{-20}, 10^{-15}] \text{ GeV}^{-1}$ and evaluate the posterior probability density $\mathcal{P}(|g_{aN}^{\text{eff}} \times g_{a\gamma\gamma}|; \text{data})$ using the `PyMultiNest` implementation of the `MultiNest` algorithm [67]. The 95% credible upper limit on $|g_{aN}^{\text{eff}} \times g_{a\gamma\gamma}|$ is then evaluated by finding the value of $|g_{aN}^{\text{eff}} \times g_{a\gamma\gamma}|$ below which 95% of the posterior probability is enclosed. Repeating this over $m_a \in [10^{-12}, 10^{-3}] \text{ eV}$ yields mass-dependent upper limits on $|g_{aN}^{\text{eff}} \times g_{a\gamma\gamma}|$. The constraints on $|g_{aN, \text{Fe}}^{\text{eff}} \times g_{a\gamma\gamma}|$ from the 14.4 keV line search from ^{57}Fe nuclear transition are shown in the left panel of Fig. 4, and those on $|g_{aN, \text{Kr}}^{\text{eff}} \times g_{a\gamma\gamma}|$ from the 9.4 keV line search from ^{83}Kr nuclear transition are shown in the left panel of Fig. 5.

We additionally derive independent constraints on the axion-photon coupling $g_{a\gamma\gamma}$ by fixing the effective axion-nucleon couplings to $g_{aN, \text{Fe}}^{\text{eff}} = 3.6 \times 10^{-6}$ and $g_{aN, \text{Kr}}^{\text{eff}} = 1.69 \times 10^{-6}$ (the value allowed by previous searches for the 9.4 keV line as given in [46]). Following the same sampling procedure to find the 95% credible upper limits, the resulting constraints on $g_{a\gamma\gamma}$ from the 14.4 keV ^{57}Fe line search are displayed in the right panel of Fig. 4. Similarly, the corresponding limits derived from the search for the 9.4 keV ^{83}Kr line are shown in the right panel of Fig. 5. In both panels of Fig. 4 and Fig. 5, the upper limits are shown using the green solid line for conservative, blue solid line for

realistic, and red dashed line for optimistic case at 95% C.L., respectively. Note that for $m_a \lesssim 10^{-6}$ eV, constraints are essentially independent of axion mass, whereas they monotonically weaken at higher masses. This behavior directly reflects that the axion-photon conversion probability in the solar atmosphere remains constant for low masses but falls rapidly for higher masses due to loss of coherence (see Fig. 2 and the discussion thereafter). Additionally, the summary of the 95% C.L. upper limits on various couplings is also provided in Table I for $m_a \lesssim 10^{-6}$ eV.

To facilitate comparison with previous results, both panels of Fig. 4 include existing limits on $|g_{aN, \text{Fe}}^{\text{eff}} \times g_{a\gamma\gamma}|$ and on $g_{a\gamma\gamma}$ (assuming $g_{aN, \text{Fe}}^{\text{eff}} = 3.6 \times 10^{-6}$) derived from 14.4 keV axion searches. These prior constraints are indicated by shaded regions, where the gray region represents the CAST experiment [43], and red represents the limits of the CUORE experiment [44]. As evident from the figure, our conservative Case 1 limit is weaker than the CUORE bound but slightly more stringent than the CAST result. In contrast, the more realistic and optimistic background subtraction schemes (Case 2 and Case 3, respectively) produce constraints that surpass both the CAST and CUORE limits.

To understand why our analysis yields competitive or strictly stronger coupling limits than CAST, it is instructive to compare the raw event limits. By treating the expected number of signal events N_S as a constant across the mass range, we find that for an observation time of $T_{\text{obs}} = 10^6$ s, our 95% C.L. upper limits for Case 1, Case 2, and Case 3 are, respectively,

$$N_S^{95} \lesssim 704, \quad 124, \quad \text{and} \quad 48. \quad (24)$$

In contrast, the CAST experiment [43] reported a stricter raw event limit of $N_S < 32$, derived from 203 hours ($\equiv 7.30 \times 10^5$ s) of Sun tracking with an effective area 29 cm^2 .

Naively, one might expect CAST's lower event count to translate directly into stronger constraints on the couplings. However, from Eq. (21) one can note that in reality N_S is a function of axion couplings and the axion-photon conversion probability $\hat{P}(E, m_a, g_{a\gamma\gamma} = 1.0)$. Thus the upper limit on the coupling relies fundamentally on the axion-photon conversion probability. The CAST Phase I data utilized for the 14.4 keV line search was taken with evacuated magnet bores, meaning the experiment relied entirely on vacuum conversion where there could be no resonance. In contrast, our search leverages conversion within the solar atmosphere (a magnetized plasma). For low axion masses, the effective photon mass in the solar atmosphere induces resonant conversion. This drastically enhances the oscillation probability, more than compensating for the XSM's smaller effective area and resulting in a stronger bound on the coupling even with our higher N_S bounds. However this advantage is highly mass-dependent.

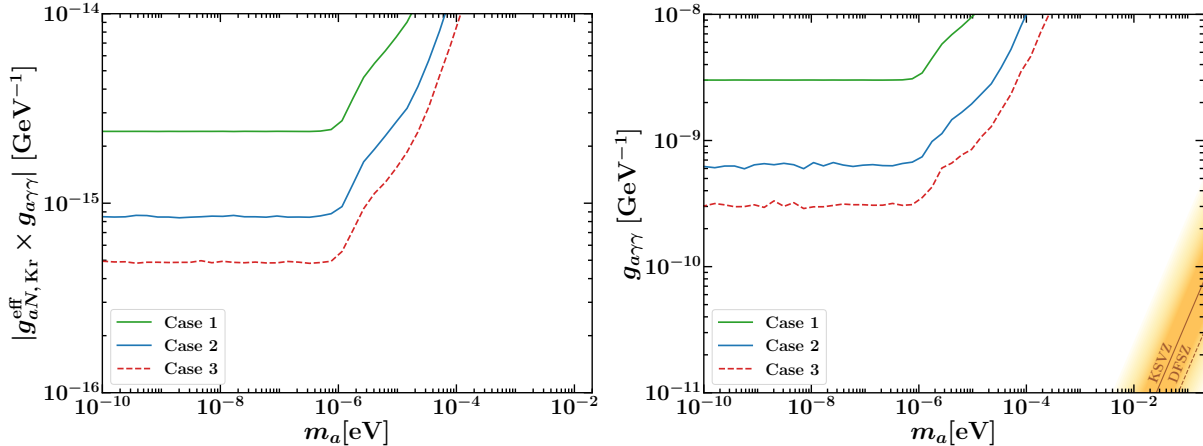


FIG. 5. Upper limits at 95% confidence level on the product $|g_{aN,Kr}^{\text{eff}} \times g_{a\gamma\gamma}|$ (left panel) and $g_{a\gamma\gamma}$ for $g_{aN,Kr}^{\text{eff}} = 1.69 \times 10^{-6}$ (right panel) as a function of the axion mass, derived from Chandrayaan-2 XSM observations. The constraint is obtained from the non-observation of an excess at the 9.4 keV ^{83}Kr nuclear transition in the solar X-ray spectrum.

| Case | ^{57}Fe | | ^{83}Kr | |
|---------------------|--------------------------------------------------------------------------------|------------------------------------------------|--------------------------------------------------------------------------------|------------------------------------------------|
| | $ g_{aN,Fe}^{\text{eff}} \times g_{a\gamma\gamma} \lesssim$ [GeV $^{-1}$] | $g_{a\gamma\gamma} \lesssim$ [GeV $^{-1}$] | $ g_{aN,Kr}^{\text{eff}} \times g_{a\gamma\gamma} \lesssim$ [GeV $^{-1}$] | $g_{a\gamma\gamma} \lesssim$ [GeV $^{-1}$] |
| Conservative | 1.2×10^{-16} | 3.5×10^{-11} | 2.5×10^{-15} | 3.0×10^{-9} |
| Realistic | 5.0×10^{-17} | 1.5×10^{-11} | 8.5×10^{-16} | 6.0×10^{-10} |
| Optimistic | 3.0×10^{-17} | 8.0×10^{-12} | 5.0×10^{-16} | 3.0×10^{-10} |

TABLE I. Summary of the 95% C.L. upper limits obtained on $|g_{aN,Fe}^{\text{eff}} \times g_{a\gamma\gamma}|$ and $g_{a\gamma\gamma}$ from the 14.4 keV line search from ^{57}Fe transition and $|g_{aN,Kr}^{\text{eff}} \times g_{a\gamma\gamma}|$ and $g_{a\gamma\gamma}$ the 9.4 keV line search from ^{83}Kr for $m_a \lesssim 10^{-6}$ eV.

As seen in Fig. 4, for $m_a \gtrsim 10^{-5}$ eV, the momentum mismatch leads to a loss of coherence in the solar atmosphere, causing the resonant oscillation probability to fall sharply. Above this threshold, our limits become considerably weaker than those of CAST, which maintains coherence over the length of its laboratory magnetic field.

Turning to the 9.4 keV line originating from the ^{83}Kr nuclear transition (Fig. 5), we found that prior constraints on the specific parameter spaces considered here ($|g_{aN,Kr}^{\text{eff}} \times g_{a\gamma\gamma}|$ and $g_{a\gamma\gamma}$) are not available in the literature. Consequently, our analysis represents the first dedicated search for 9.4 keV solar axions utilizing this channel. The only existing limit related to this transition is reported by Gavriluk *et al.* [46], which placed an upper bound solely on the effective axion-nucleon coupling, finding $g_{aN,Kr}^{\text{eff}} < 1.69 \times 10^{-6}$ at 95% C.L. for axion masses $m_a < 130$ eV.

V. RESULTS AND DISCUSSION

In this work, we have investigated the production of monoenergetic solar axions via the M1 nuclear de-excitation of ^{57}Fe and ^{83}Kr , emitting at 14.4 keV and 9.4 keV, respectively. These axions can subsequently convert into X-ray photons in the solar magnetic field via the inverse Primakoff process, yielding a sharp spectral line observable by X-ray telescopes. Using solar soft X-ray data from Chandrayaan-2 XSM, we have derived constraints on the product of the effective axion-nucleon and axion-photon couplings, $|g_{aN}^{\text{eff}} \times g_{a\gamma\gamma}|$ and only axion-photon coupling $g_{a\gamma\gamma}$ for a fixed g_{aN}^{eff} , across three background subtraction schemes, which we refer to as conservative, realistic, and optimistic. For a summary, see the second and third columns of Table I for ^{57}Fe . The conservative bound is comparable to existing constraints from CAST and CUORE, while the realistic and optimistic cases surpass them. Despite XSM's smaller effective area compared to CAST, we find that the longer solar observation time and enhanced conversion probability arising from resonant conversion in the solar atmosphere yield stronger limits in both the realistic and optimistic cases.

For ^{83}Kr (see 4th and 5th columns Table I), these bounds are weaker than those from ^{57}Fe by more than an order of magnitude, a direct consequence of the lower solar abundance of krypton, which suppresses the ^{83}Kr axion flux by nearly three orders of magnitude as discussed in Sec. II. The effective axion-nucleon couplings for the two isotopes, $g_{aN, \text{Fe}}^{\text{eff}} = -1.19 g_{0aN} + g_{3aN}$ and $g_{aN, \text{Kr}}^{\text{eff}} = -g_{0aN} + g_{3aN}$, are numerically similar but slightly different linear combinations of the isoscalar and isovector nucleon couplings. Taken together, the two lines therefore offer complementary sensitivity to the axion-nucleon parameter space.

Finally, these results demonstrate that solar X-ray observations with Chandrayaan-2 provide a competitive and independent probe of axion models, with the sensitivity strongly dependent on the choice of background model. Future observations with next-generation solar X-ray instruments, combined with improved solar magnetic field models, could further sharpen these constraints and probe regions of the axion parameter space currently beyond the reach of laboratory experiments.

ACKNOWLEDGMENTS

The authors thank Maurizio Giannotti for his insightful comments, which helped to improve the manuscript significantly. The authors gratefully acknowledge Santosh Vadawale, N. P. S. Mithun, and B. S. Bharath Saiguan for providing the reduced Chandrayaan-2 dataset utilized in this analysis. The authors are also grateful to the organizers of the Workshop in High Energy Physics

(WHEPP) 2025 at Indian Institute of Technology Hyderabad, where this work was initiated. TK would also like to acknowledge support in the form of a Senior Research Fellowship from the Council of Scientific & Industrial Research (CSIR), Government of India.

-
- [1] R. D. Peccei and H. R. Quinn, CP Conservation in the Presence of Instantons, *Phys. Rev. Lett.* **38**, 1440 (1977).
 - [2] F. Wilczek, Problem of Strong P and T Invariance in the Presence of Instantons, *Phys. Rev. Lett.* **40**, 279 (1978).
 - [3] S. Weinberg, A New Light Boson?, *Phys. Rev. Lett.* **40**, 223 (1978).
 - [4] M. Dine and W. Fischler, The Not So Harmless Axion, *Phys. Lett. B* **120**, 137 (1983).
 - [5] L. F. Abbott and P. Sikivie, A Cosmological Bound on the Invisible Axion, *Phys. Lett. B* **120**, 133 (1983).
 - [6] J. Preskill, M. B. Wise, and F. Wilczek, Cosmology of the Invisible Axion, *Phys. Lett. B* **120**, 127 (1983).
 - [7] R. L. Davis, Cosmic Axions from Cosmic Strings, *Phys. Lett. B* **180**, 225 (1986).
 - [8] J. E. Kim and G. Carosi, Axions and the Strong CP Problem, *Rev. Mod. Phys.* **82**, 557 (2010), [Erratum: *Rev. Mod. Phys.* 91, 049902 (2019)], [arXiv:0807.3125 \[hep-ph\]](#).
 - [9] D. J. E. Marsh, Axion Cosmology, *Phys. Rept.* **643**, 1 (2016), [arXiv:1510.07633 \[astro-ph.CO\]](#).
 - [10] C. B. Adams *et al.*, Axion Dark Matter, in *2022 Snowmass Summer Study* (2022) [arXiv:2203.14923 \[hep-ex\]](#).
 - [11] M. Baryakhtar *et al.*, Dark Matter In Extreme Astrophysical Environments, in *2022 Snowmass Summer Study* (2022) [arXiv:2203.07984 \[hep-ph\]](#).
 - [12] L. Di Luzio, M. Giannotti, E. Nardi, and L. Visinelli, The landscape of QCD axion models, *Phys. Rept.* **870**, 1 (2020), [arXiv:2003.01100 \[hep-ph\]](#).
 - [13] J. Jaeckel and A. Ringwald, The Low-Energy Frontier of Particle Physics, *Ann. Rev. Nucl. Part. Sci.* **60**, 405 (2010), [arXiv:1002.0329 \[hep-ph\]](#).
 - [14] M. Giannotti, I. G. Irastorza, J. Redondo, A. Ringwald, and K. Saikawa, Stellar Recipes for Axion Hunters, *JCAP* **10**, 010, [arXiv:1708.02111 \[hep-ph\]](#).
 - [15] P. Agrawal *et al.*, Feebly-interacting particles: FIPs 2020 workshop report, *Eur. Phys. J. C* **81**, 1015 (2021), [arXiv:2102.12143 \[hep-ph\]](#).
 - [16] L. Di Luzio, M. Fedele, M. Giannotti, F. Mescia, and E. Nardi, Stellar evolution confronts axion models, *JCAP* **02** (02), 035, [arXiv:2109.10368 \[hep-ph\]](#).
 - [17] M. Giannotti, Exciting times, *Nature Phys.* **13**, 530 (2017).
 - [18] M. Giannotti, Aspects of Axions and ALPs Phenomenology, in *10th Symposium on Large TPCs for Low-Energy Rare Event Detection* (2022) [arXiv:2205.06831 \[hep-ph\]](#).

- [19] I. G. Irastorza and J. Redondo, New experimental approaches in the search for axion-like particles, *Prog. Part. Nucl. Phys.* **102**, 89 (2018), arXiv:1801.08127 [hep-ph].
- [20] P. Di Vecchia, M. Giannotti, M. Lattanzi, and A. Lindner, Round Table on Axions and Axion-like Particles, *PoS Confinement2018*, 034 (2019), arXiv:1902.06567 [hep-ph].
- [21] P. Sikivie, Invisible Axion Search Methods, *Rev. Mod. Phys.* **93**, 015004 (2021), arXiv:2003.02206 [hep-ph].
- [22] A. Arza *et al.*, The cosmic wispers white paper: The physics case for weakly interacting slim particles (2026), arXiv:2603.03433 [hep-ph].
- [23] C. O’Hare, *cajohare/axionlimits: Axionlimits*, <https://cajohare.github.io/AxionLimits/> (2020).
- [24] G. G. Raffelt, ASTROPHYSICAL AXION BOUNDS DIMINISHED BY SCREENING EFFECTS, *Phys. Rev. D* **33**, 897 (1986).
- [25] G. G. Raffelt, Plasmon Decay Into Low Mass Bosons in Stars, *Phys. Rev. D* **37**, 1356 (1988).
- [26] A. Caputo, A. J. Millar, and E. Vitagliano, Revisiting longitudinal plasmon-axion conversion in external magnetic fields, *Phys. Rev. D* **101**, 123004 (2020), arXiv:2005.00078 [hep-ph].
- [27] C. A. J. O’Hare, A. Caputo, A. J. Millar, and E. Vitagliano, Axion helioscopes as solar magnetometers, *Phys. Rev. D* **102**, 043019 (2020), arXiv:2006.10415 [astro-ph.CO].
- [28] E. Guarini, P. Carena, J. Galan, M. Giannotti, and A. Mirizzi, Production of axionlike particles from photon conversions in large-scale solar magnetic fields, *Phys. Rev. D* **102**, 123024 (2020), arXiv:2010.06601 [hep-ph].
- [29] J. Redondo, Solar axion flux from the axion-electron coupling, *JCAP* **12**, 008, arXiv:1310.0823 [hep-ph].
- [30] S. Hoof, J. Jaeckel, and L. J. Thormaehlen, Quantifying uncertainties in the solar axion flux and their impact on determining axion model parameters, *JCAP* **09**, 006, arXiv:2101.08789 [hep-ph].
- [31] V. Anastassopoulos *et al.* (CAST), New CAST Limit on the Axion-Photon Interaction, *Nature Phys.* **13**, 584 (2017), arXiv:1705.02290 [hep-ex].
- [32] A. Ayala, I. Domínguez, M. Giannotti, A. Mirizzi, and O. Straniero, Revisiting the bound on axion-photon coupling from Globular Clusters, *Phys. Rev. Lett.* **113**, 191302 (2014), arXiv:1406.6053 [astro-ph.SR].
- [33] O. Straniero, A. Ayala, M. Giannotti, A. Mirizzi, and I. Dominguez, Axion-Photon Coupling: Astrophysical Constraints, in *11th Patras Workshop on Axions, WIMPs and WISPs* (2015) pp. 77–81.
- [34] M. J. Dolan, F. J. Hiskens, and R. R. Volkas, Advancing globular cluster constraints on the axion-photon coupling, *JCAP* **10**, 096, arXiv:2207.03102 [hep-ph].
- [35] T. W. Donnelly, S. J. Freedman, R. S. Lytel, R. D. Peccei, and M. Schwartz, Do Axions Exist?, *Phys. Rev. D* **18**, 1607 (1978).
- [36] R. Massarczyk, P. H. Chu, and S. R. Elliott, Axion emission from nuclear magnetic dipole transitions, *Phys. Rev. D* **105**, 015031 (2022), arXiv:2112.08285 [hep-ph].
- [37] A. V. Derbin, A. I. Egorov, I. A. Mitropolsky, and V. N. Muratova, Search for solar axions emitted in an M1 transition in Li-7 nuclei, *JETP Lett.* **81**, 365 (2005).

- [38] P. Belli *et al.*, Li-7 solar axions: Preliminary results and feasibility studies, *Nucl. Phys. A* **806**, 388 (2008).
- [39] G. Bellini *et al.* (Borexino), Search for solar axions emitted in the M1-transition of Li-7* with Borexino CTF, *Eur. Phys. J. C* **54**, 61 (2008).
- [40] S. Andriamonje *et al.* (CAST), Search for solar axion emission from ${}^7\text{Li}$ and $D(p, \gamma){}^3\text{He}$ nuclear decays with the CAST γ -ray calorimeter, *JCAP* **03**, 032, arXiv:0904.2103 [hep-ex].
- [41] S. Moriyama, A Proposal to search for a monochromatic component of solar axions using Fe-57, *Phys. Rev. Lett.* **75**, 3222 (1995), arXiv:hep-ph/9504318.
- [42] M. Krcmar, Z. Krecak, M. Stipcevic, A. Ljubicic, and D. A. Bradley, Search for invisible axions using Fe-57, *Phys. Lett. B* **442**, 38 (1998), arXiv:nucl-ex/9801005.
- [43] S. Andriamonje *et al.* (CAST), Search for 14.4-keV solar axions emitted in the M1-transition of Fe-57 nuclei with CAST, *JCAP* **12**, 002, arXiv:0906.4488 [hep-ex].
- [44] F. Alessandria *et al.* (CUORE), Search for 14.4 keV solar axions from M1 transition of Fe-57 with CUORE crystals, *JCAP* **05**, 007, arXiv:1209.2800 [hep-ex].
- [45] K. Jakovcic, Z. Krecak, M. Krcmar, and A. Ljubicic, A Search for solar hadronic axions using ${}^{83}\text{Kr}$, *Radiat. Phys. Chem.* **71**, 793 (2004), arXiv:nucl-ex/0402016.
- [46] Y. M. Gavrilyuk *et al.*, First result of the experimental search for the 9.4 keV solar axion reactions with ${}^{83}\text{Kr}$ in the copper proportional counter, *Phys. Part. Nucl.* **46**, 152 (2015), arXiv:1405.1271 [nucl-ex].
- [47] L. Di Luzio *et al.*, Probing the axion–nucleon coupling with the next generation of axion helioscopes, *Eur. Phys. J. C* **82**, 120 (2022), arXiv:2111.06407 [hep-ph].
- [48] A. Bhusal, N. Houston, and T. Li, Searching for Solar Axions Using Data from the Sudbury Neutrino Observatory, *Phys. Rev. Lett.* **126**, 091601 (2021), arXiv:2004.02733 [hep-ph].
- [49] G. Raffelt and L. Stodolsky, New Particles From Nuclear Reactions in the Sun, *Phys. Lett. B* **119**, 323 (1982).
- [50] G. Bellini *et al.* (Borexino), Search for Solar Axions Produced in $p(d, {}^3\text{He})\text{A}$ Reaction with Borexino Detector, *Phys. Rev. D* **85**, 092003 (2012), arXiv:1203.6258 [hep-ex].
- [51] G. Lucente, N. Nath, F. Capozzi, M. Giannotti, and A. Mirizzi, Probing high-energy solar axion flux with a large scintillation neutrino detector, *Phys. Rev. D* **106**, 123007 (2022), arXiv:2209.11780 [hep-ph].
- [52] M. Asplund, A. M. Amarsi, and N. Grevesse, The chemical make-up of the Sun: A 2020 vision, *Astron. Astrophys.* **653**, A141 (2021), arXiv:2105.01661 [astro-ph.SR].
- [53] S. V. Vadawale *et al.*, Observations of the Quiet Sun during the Deepest Solar Minimum of the Past Century with Chandrayaan-2 XSM: Elemental Abundances in the Quiescent Corona, *Astrophys. J. Lett.* **912**, L12 (2021), arXiv:2103.16643 [astro-ph.SR].
- [54] S. V. Vadawale *et al.*, Observations of the Quiet Sun during the Deepest Solar Minimum of the Past Century with Chandrayaan-2 XSM: Sub-A-class Microflares outside Active Regions, *Astrophys. J. Lett.* **912**, L13 (2021), arXiv:2103.16644 [astro-ph.SR].

- [55] T. Kumar, N. P. S. Mithun, S. Mohanty, S. Roy, B. S. B. Saiguhan, and S. Vadawale, Limits on the axion-photon coupling from Chandrayaan-2 observations, *Phys. Rev. D* **113**, L061303 (2026), [arXiv:2510.06087 \[hep-ph\]](#).
- [56] J. Ruz *et al.*, NuSTAR as an Axion Helioscope, *Phys. Rev. Lett.* **135**, 141001 (2025), [arXiv:2407.03828 \[astro-ph.CO\]](#).
- [57] F. T. Avignone, C. Baktash, W. C. Barker, F. P. Calaprice, R. W. Dunford, W. C. Haxton, D. Kahana, R. T. Kouzes, H. S. Miley, and D. M. Moltz, Search for Axions From the 1115-keV Transition of ^{65}Cu , *Phys. Rev. D* **37**, 618 (1988).
- [58] Y. Herrera and A. Serenelli, Standard solar models B23 / SF-III (v1.2), [10.5281/zenodo.10822316](#) (2023).
- [59] G. Raffelt and L. Stodolsky, Mixing of the Photon with Low Mass Particles, *Phys. Rev. D* **37**, 1237 (1988).
- [60] C. A. Manzari, Y. Park, B. R. Safdi, and I. Savoray, Supernova Axions Convert to Gamma Rays in Magnetic Fields of Progenitor Stars, *Phys. Rev. Lett.* **133**, 211002 (2024), [arXiv:2405.19393 \[hep-ph\]](#).
- [61] R. P. Dufresne, G. Del Zanna, P. R. Young, K. P. Dere, E. Deliporanidou, W. T. Barnes, and E. Landi, CHIANTI—An Atomic Database for Emission Lines—Paper. XVIII. Version 11, Advanced Ionization Equilibrium Models: Density and Charge Transfer Effects, *Astrophys. J.* **974**, 71 (2024), [arXiv:2403.16922 \[astro-ph.SR\]](#).
- [62] G. Del Zanna, K. P. Dere, P. R. Young, and E. Landi, CHIANTI—An Atomic Database for Emission Lines. XVI. Version 10, Further Extensions, *Astrophys. J.* **909**, 38 (2021), [arXiv:2011.05211 \[physics.atom-ph\]](#).
- [63] Chiantipy, <https://github.com/chianti-atomic/ChiantiPy/> (2022).
- [64] M. Berger, J. Hubbell, S. Seltzer, J. Chang, J. Coursey, R. Sukumar, D. Zucker, and K. Olsen, Xcom: Photon cross sections database, <https://www.nist.gov/pml/xcom-photon-cross-sections-database>.
- [65] M. Shanmugam, S. V. Vadawale, A. R. Patel, H. K. Adalaja, N. P. S. Mithun, T. Ladiya, S. K. Goyal, N. K. Tiwari, N. Singh, S. Kumar, D. K. Painkra, Y. B. Acharya, A. Bhardwaj, A. K. Hait, A. Patinge, A. Kapoor, H. N. S. Kumar, N. Satya, G. Saxena, and K. Arvind, Solar X-ray Monitor onboard Chandrayaan-2 Orbiter, *Current Science* **118**, 45 (2020), [arXiv:1910.09231 \[astro-ph.IM\]](#).
- [66] N. P. S. Mithun *et al.*, Solar X-Ray Monitor on Board the Chandrayaan-2 Orbiter: In-Flight Performance and Science Prospects, *Sol. Phys.* **295**, 139 (2020), [arXiv:2009.09759 \[astro-ph.SR\]](#).
- [67] F. Feroz, M. P. Hobson, and M. Bridges, MultiNest: an efficient and robust Bayesian inference tool for cosmology and particle physics, *Mon. Not. Roy. Astron. Soc.* **398**, 1601 (2009), [arXiv:0809.3437 \[astro-ph\]](#).